Optimal Bandwidth Positions for a Terminal Embedded Antenna: Physical Bounds and Antenna Design

B. L. G. Jonsson, Fabien Ferrero, *Senior Member, IEEE*, Shuai Shi, and Lei Wang, *Senior Member, IEEE*

***Abstract*— This article considers a small embedded planar antenna in a square-shaped terminal of 25 cm^2 at a frequency band near 900 MHz, intended for long-range communication. This article aims to shows how the Q-factor bounds can be used to predict the performance of such an antenna. Both to determine the optimal bandwidth and the variations in the total efficiency but also to help to inspire the antenna design shape. The choice of shape and position impacts both bandwidth and efficiency. The latter is illustrated by a center-edge positioned folded inverted F-antenna with higher efficiency, as compared to, a more bandwidth optimal meander antenna at the corner. Fabrication and measurements show that the corner positioned antenna is close to bandwidth optimal, and also that it and the associated optimal current have a similar radiation pattern.**

***Index Terms*— Bandwidth, current optimization, embedded antenna, optimization, Q-factor.**

I. Introduction

SMALL antennas are increasingly used in almost every connected electronic device, such as cell phones, sensors, trackers, Internet of Things (IoT), and machine-to-machine (M2M) communication devices [1]–[6]. These antennas are embedded as a part of the terminal or its chassis. The position of the embedded antenna is known to impact its bandwidth, efficiency, and far-field pattern. In this article, a Q-factor bound is used to determine the optimal position of a small antenna embedded in a 5 × 5 cm terminal. The optimality here is with respect to the smallest antenna Q-factor, that is closely associated with the available impedance bandwidth.

The bandwidth requirement of an embedded antenna is often rather small. For example, devices that operate in one of the free industry-scientific-medical (ISM) bands have a fractional bandwidth (FBW) of 3% or less. In Europe, the short-range device (SRD) 868 MHz has an FBW of 1%. However, different ISM bands are used all over the world, 915 MHz in USA or 923 MHz in Asia, thus a worldwide IoT system should have a 7% FBW centered at 895 MHz. Moreover, there is also a drive to deploy M2M and IoT devices within the long-term evolution (LTE) frequency bands as defined in e.g., the LTE-M or LTE-NB standards [7]. Here, the individual communication channel is narrowband but the bandwidth of the device has to be larger because of the frequency division duplex (FDD) scheme since a channel can appear anywhere within the frequency bands defined by the LTE-M/LTE-NB-standards. As an example, the band number 20 from 3GPP will require an 8% FBW centered at 826 MHz.

Given the fact that the physical size is a limiting factor for small antennas, it is important and interesting to determine the physical limits of the largest possible bandwidth for embedded antennas. This is, in particular, the case in small low-frequency devices with an expected larger communication range (see [3], [8]). To determine the best antenna bandwidth, we use the stored energy Q-factor [9], which is known to provide an accurate estimation of the bandwidth for electrically small antennas [10], [11], see also [12]–[14] for periodic structures. The optimal antenna bandwidth can be increased, for example, by allowing a larger antenna size, or by adding a matching network beyond a tuning element in which the antenna together with the matching network has a wider bandwidth. Such considerations are normally done after the available antenna bandwidth is determined.

Stored energies, as defined in [9], [15], and [16] are utilized here since they allow antenna-current optimization [17], [18]. Such optimization can provide bandwidth bounds for small arbitrary-shaped antenna domains. Antenna-current optimization has successfully been applied to determine bounds on a range of antenna parameters. It was first used to determine the ratio of partial directivity over Q (see [17], [19]). Recently, optimization of the Q-factor as a pareto-front with demands of increasing directivity was considered in [18].

Manuscript received August 22, 2019; revised August 7, 2020; accepted August 29, 2020. Date of publication October 1, 2020; date of current version April 7, 2021. This work was supported in part by the Swedish Foundation for Strategic Research through the Project Convex Analysis and Convex Optimization for EM Design under Grant SSF/AM130011 and in part by the Swedish Governmental Agency for Innovation Systems through the Center ChaseOn in the Project iAA under Grant ChaseOn/iAA. The work of Shuai Shi was supported by the China Scholarship Council (CSC). *(Corresponding author: B. L. G. Jonsson.)*

B. L. G. Jonsson is with the Electromagnetic Engineering Laboratory, School of Electrical Engineering and Computer Science, KTH Royal Institute of Technology, SE-100 44 Stockholm, Sweden (e-mail: ljonsson@kth.se).

Fabien Ferrero is with the Laboratoire d'Electronique, Antennes et Télécommunications (LEAT), National Center for Scientific Research (CNRS), Université Côte d'Azur, 06903 Sophia Antipolis, France.

Shuai Shi is with Ericsson AB, SE-164 80 Stockholm, Sweden.

Lei Wang is with the School of Engineering and Physical Sciences, Institute of Sensors, Signals and Systems, Heriot-Watt University, Edinburgh EH14 4AS, U.K.

Color versions of one or more of the figures in this article are available online at https://ieeexplore.ieee.org.

Digital Object Identifier 10.1109/TAP.2020.3026921

Current optimization was applied to optimize antenna gain in [20] and to determine bounds on the Q-factor for a given power front-to-back ration [21]. Capacity for MIMO-antennas under different constraints has also been considered [22], [23]. Fundamental bounds for antenna efficiency and the Q-factor for lossy structures have been considered in [24] and [25]. Other approaches to fundamental bounds for losses include [26]–[28].

In this article, we determine the optimal position in an electrically small planar device and study how "frequency-stable" the predicted optimal position is. The antenna efficiency associated with the optimal bandwidth currents is also determined. The results are compared with antenna designs, whereof one of the designs is inspired by a minimizing current. Two different antennas are fabricated and measured. The measurements are compared with the physical bounds for two different embedded positions. Other investigations of antennas that approach physical bounds include [18], [21], and [29]–[31] (see also [32]–[36]).

The current optimization approach used here to determine the Q-factor bounds is, as an optimization problem, a quadratically constrained quadratic program (QCQP). These types of problems frequently come with nonconvex constraints. However, with few enough constraints, such QCQP:s have a globally unique solution [37]. The solution methods include the semi-definite relaxation (SDR) technique [38], [39], a dual-based eigenvalue method (see [18], [40]–[42]). The presented solutions are mainly based on an in-house dual-based eigenvalue optimization method (see [43]).

The rest of this article is organized as follows: In Section II we introduce the antenna geometry and briefly recall how the Q-factor and other antenna quantities are expressed in a method of moment (MoM) setting. We close this section by posing the optimization problem for determining the minimal Q-factor as a function of the embedded antenna position. This is followed in Section III by the analysis of the optimization results. Three different cases are considered: how the bandwidth depends on the embedded position, changes of efficiency associated with the optimal current at each position, and how frequency-stable the optimal position is. Section IV presents the simulation and analysis of the antenna design, the manufacturing, and the measurement procedure. In Section V, we compare and discuss the obtained bounds with the measured results. This article ends with conclusions.

II. Theory

A. Problem Description

A small IoT terminal of negligible height is considered here. It is approximated by a 5×5 cm planar square metal-surface, Ω. The embedded antenna is to be designed in a 2×2 cm region, Ω_2, within the terminal (see Fig. 1). The terminal size is smaller than a mobile phone, but still large enough to support antennas with enough bandwidth for the sub-GHz SRD and ISM frequency bands (868, 915, and 923 MHz) together with space for electronics, batteries, and other accessories like sensors or a display. Access to other frequency bands like the GPS-bands and WiFi is also

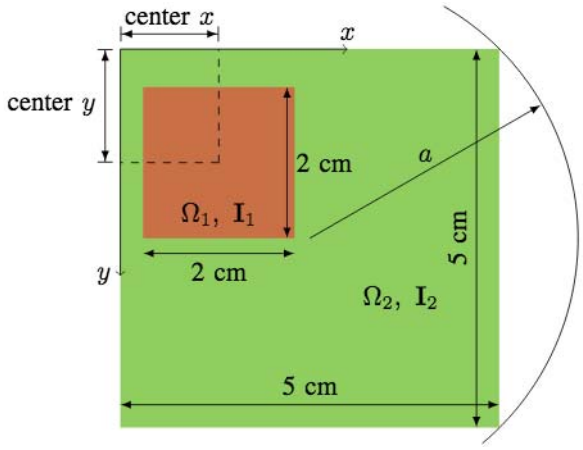

Fig. 1. Embedded antenna, Ω_1, (brown) within the terminal $\Omega = \Omega_1 + \Omega_2$. The terminal can be enclosed in a sphere with radius a.

interesting. Here, the focus is mainly on the lower frequency bands. They are constrained in bandwidth as the terminal is electrically small, $ka \sim 0.67$ at 900 MHz, where a is the radius of an enclosing sphere and k is the wavenumber. The FBW for electrically small antennas are closely related to the antenna Q-factor, Q

$$\text{FBW} = \frac{f_2 - f_1}{f_0} \approx \frac{2|\Gamma_0|}{Q\sqrt{1 - |\Gamma_0|^2}} \tag{1}$$

where $f_0 = (f_1 + f_2)/2$ is the center frequency, and $|\Gamma_0|$ denotes the maximally allowed reflection coefficient.

The Q-factor approach to estimate bandwidth shows that it is sufficient to determine the smallest Q-factor, to find the widest bandwidth. The tuned Q-factor is defined by

$$Q = \frac{2\omega \max(W_\text{e}, W_\text{m})}{P_\text{rad} + P_\text{d}} = eQ_\text{rad} \tag{2}$$

where ω is the angular frequency, W_e and W_m are the electric and magnetic stored energy, respectively. Furthermore, P_rad is the radiated power of the antenna, and P_d is the dissipated power. Let Q_rad denote the radiated Q-factor and $e = P_\text{rad}/(P_\text{rad} + P_\text{d})$ is the antenna efficiency [11], [15], [16], [19]. Furthermore, P_rad is the radiated power of the antenna, P_d is the dissipated power. Let Q_rad denote the radiated Q-factor and $e = P_\text{rad}/(P_\text{rad} + P_\text{d})$ is the efficiency.

An advantage of using stored energy instead of, for example, the input impedance to determine the Q-factor is, that such a representation can be bounded from below by current optimization. Thus, it can be used to predict the best available Q-factor of any antenna in the considered region. That is, given a maximal allowed reflection coefficient, there is an upper bound on the bandwidth of all lossless passive antenna that fits in the proposed region [17].

B. Representation of Antenna Parameters

The optimal Q-factor is here determined numerically through an MoM approach using the Rao–Wilton–Glisson (RWG) basis functions [44]. Denote an RWG-basis function with $\boldsymbol{\psi}_n$, and the set of N such basis functions are then denoted

by $\{\boldsymbol{\psi}_n\}_{n=1}^N$. The surface current, $\boldsymbol{J}$, in the region Ω at the position $\boldsymbol{r} \in \Omega$ is approximated by

$$\boldsymbol{J}(\boldsymbol{r}) \approx \sum_{n=1}^{N} I_n \boldsymbol{\psi}_n(\boldsymbol{r}). \tag{3}$$

The current coefficients $\{I_n\}_{n=1}^N$ are gathered as an $N \times 1$ vector, $\mathbf{I}$. This facilitates the representation of the electric field integral operator an impedance matrix $\mathbf{Z} = \mathbf{R} + \mathrm{j}\mathbf{X} \in \mathbb{C}^{N\times N}$ for the region Ω [44]. The associated matrix representation, $\mathbf{X}_\mathrm{e}, \mathbf{X}_\mathrm{m} \in \mathbb{R}^{N\times N}$, of the electric and magnetic stored energy are [45]

$$W_\mathrm{e} \approx \frac{1}{8}\mathbf{I}^H\left(\frac{\partial \mathbf{X}}{\partial \omega} - \frac{\mathbf{X}}{\omega}\right)\mathbf{I} = \frac{1}{4\omega}\mathbf{I}^H\mathbf{X}_\mathrm{e}\mathbf{I} \tag{4}$$

$$W_\mathrm{m} \approx \frac{1}{8}\mathbf{I}^H\left(\frac{\partial \mathbf{X}}{\partial \omega} + \frac{\mathbf{X}}{\omega}\right)\mathbf{I} = \frac{1}{4\omega}\mathbf{I}^H\mathbf{X}_\mathrm{m}\mathbf{I}. \tag{5}$$

Here, $\cdot^H$ denote the Hermite conjugate. The radiated power from the antenna is

$$P_\mathrm{rad} \approx \frac{1}{2}\mathbf{I}^H\mathbf{R}\mathbf{I}. \tag{6}$$

The dissipated power in the terminal can for a good conductor be estimated in terms of an equivalent surface current density and a surface resistance, R_s, as $P_\mathrm{d} \approx \frac{R_\mathrm{s}}{2}\int_\Omega |\boldsymbol{J}|^2 \,\mathrm{d}S$ (see [24], [25], [46]). The surface resistivity used here is the two-sided resistivity $R_\mathrm{s} = (2\sigma d)^{-1}$ since the terminal has currents on both sides of the conductor. Above, σ is the conductivity and d is the skin-depth. In the RWG-representation the dissipative power reduces to

$$P_\mathrm{d} \approx \frac{R_\mathrm{s}}{2}\int_\Omega |\boldsymbol{J}|^2 \,\mathrm{d}S \approx \frac{R_\mathrm{s}}{2}\mathbf{I}^H\Psi\mathbf{I} \tag{7}$$

which follows by a substitution of (3) into (7). Here, Ψ is the Gram matrix with elements $\{\Psi_{mn}\}_{m,n=1}^N$ defined by

$$\Psi_{mn} = \int_\Omega \boldsymbol{\psi}_m(\boldsymbol{r}) \cdot \boldsymbol{\psi}_n(\boldsymbol{r}) \,\mathrm{d}S, \quad m, n \in [1, N]. \tag{8}$$

The antenna efficiency, e, is represented as

$$e = \frac{P_\mathrm{rad}}{P_\mathrm{rad} + P_\mathrm{d}} = \frac{1}{1+\delta} \approx \frac{\mathbf{I}^H\mathbf{R}\mathbf{I}}{\mathbf{I}^H(\mathbf{R} + R_\mathrm{s}\Psi)\mathbf{I}} \tag{9}$$

where δ is the dissipation factor [47]

$$\delta = \frac{P_\mathrm{d}}{P_\mathrm{rad}} = \frac{1}{e} - 1. \tag{10}$$

With the above representations, all terms in (2) are known. An optimization over all current vectors in the RWG-representation of (2) determines a lower Q-factor bound for antennas utilizing the whole domain Ω. To account for the embedding of the antenna to the region Ω_1, it is assumed that the current coefficient vector, $\mathbf{I}_2$, associated with $\Omega_2 = \Omega\backslash\Omega_1$ is induced from currents, $\mathbf{I}_1$, in Ω_1. The region partitioning also partitions of the impedance matrix into block-matrices $\mathbf{Z}_{mn}$, $m, n \in [1, 2]$. The induced currents are determined by a metal-boundary condition [17], [48] on Ω_2, thus

$$\mathbf{Z}_{21}\mathbf{I}_1 + \mathbf{Z}_{22}\mathbf{I}_2 = \mathbf{0} \;\Rightarrow\; \mathbf{I}_2 = -\mathbf{Z}_{22}{}^{-1}\mathbf{Z}_{21}\mathbf{I}_1 = \mathbf{C}\mathbf{I}_1. \tag{11}$$

Introducing this representation for I_2 in (4)–(7) results in a reduced $M \times M$ version of the matrices $\mathbf{X}_\mathrm{e}$, $\mathbf{X}_\mathrm{m}$, $\mathbf{R}$, and Ψ, denoted by a $\tilde{\cdot}$ that act only upon $\mathbf{I}_1$

$$\tilde{\mathbf{X}} = \mathbf{X}_{11} + \mathbf{X}_{12}\mathbf{C} + \mathbf{C}^H\mathbf{X}_{21} + \mathbf{C}^H\mathbf{X}_{22}\mathbf{C}. \tag{12}$$

This reduction technique is analogous to a special case of the numerical Green's function [49]. The induced current $\mathbf{I}_2$ on Ω_2 is uniquely determined by (11). The induction matrix, $\mathbf{C}$, thus effectively reduces all antenna quantities to smaller matrices acting on $\mathbf{I}_1$, through (12). The embedded region, as a part of the terminal, has a bound from below on the Q-factor that can be expressed in terms of the stored energies and total power as before but, now expressed in terms of the reduced matrices. All considerations below are formulated in terms of the reduced matrices and the tilde, $\tilde{\cdot}$, is dropped to increase the clarity of the presentation. These matrices are in the here considered problems determined by an in-house MoM code.

C. Minimizing Q

The lower bound on Q_rad for each position of the embedded antenna is determined by solving the RWG-representation of the optimization problem $Q_\mathrm{rad} = \min_{\mathbf{I}_1} \max(\mathbf{I}_1^H\mathbf{X}_\mathrm{e}\mathbf{I}_1, \mathbf{I}_1^H\mathbf{X}_\mathrm{m}\mathbf{I}_1)/(\mathbf{I}_1^H\mathbf{R}\mathbf{I}_1)$ subject to the efficiency constraint $e(\mathbf{I}_1) \le (1+\delta_0)^{-1}$ for a worst case dissipation factor δ_0. The underlying idea [17] for obtaining a lower Q-factor bound is that the optimization is over all possible currents in Ω_1. They will thus include any realized antenna geometry and its associated current within Ω_1. To simplify, note that this optimization problem is scaling invariant under the transform $\mathbf{I}_1 \mapsto \alpha\mathbf{I}_1$, for $\alpha \in \mathbb{C}$. By a choice of scaling, α, such that $\mathbf{I}_1^H\mathbf{R}\mathbf{I}_1 = 1$, which corresponds to studying all currents for which the terminal radiate $\frac{1}{2}$W, the optimization problem reduce to

$$\begin{aligned} Q_\mathrm{rad} = \min_{\mathbf{I}_1 \in \mathbb{C}^M} & \max\{\mathbf{I}_1^H\mathbf{X}_\mathrm{e}\mathbf{I}_1, \mathbf{I}_1^H\mathbf{X}_\mathrm{m}\mathbf{I}_1\} \\ \text{s.t } & \mathbf{I}_1^H\mathbf{R}\mathbf{I}_1 = 1 \\ & \mathbf{I}_1^H\Psi\mathbf{I}_1 \le \frac{\delta_0}{R_\mathrm{s}} \end{aligned} \tag{13}$$

for an efficiency equal or better than $(1+\delta_0)^{-1}$. Above, $M \le N$ is the number of basis functions in the embedded current vector $\mathbf{I}_1$. Note that an inactive dissipation-factor constraint in (13) results in that the solution has what is here called a default efficiency (see Section III-B). Removing the δ_0-constraint results in an optimization problem that is identical to the optimization of lossless antennas, thus $Q_\mathrm{lossless} = Q_\mathrm{rad}$, for large enough δ_0.

The optimization problem (13) is called a QCQP (see [42]). The matrices involved are symmetric and positive semi-definite for electrically small antennas. In this article, two different methods are used to solve (13). They are the SDR [18], [21], [38] and a Lagrangian-based eigenvalue approach [18], [40]. In the SDR approach, it is easy to add constraints with little or no additional complexity. However, with three or more constraints [37] it is no longer possible to guarantee that the semi-definite relaxed method yields the unique minimum, but rather a lower bound on the minimum [39]. For (13),

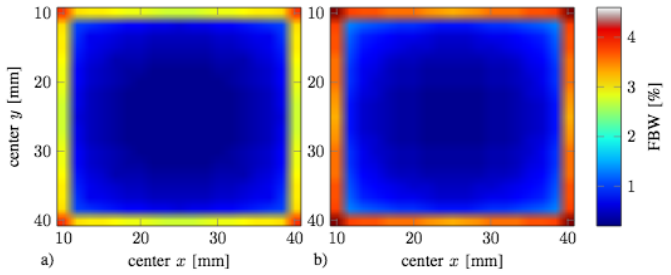

Fig. 2. Color at the depicted center-positions indicate the FBW of a 2×2 cm^2 embedded antenna with reflection coefficient $|\Gamma| \leq 1/\sqrt{2}$ at (a) 850 and (b) 900 MHz for each center position of the embedded antenna.

both methods give the same unique minimum, and it is straightforward to determine the best Q-factor.

III. Optimal Position—Bounds

A. Bandwidth Best Positions Near 900 MHz

To determine the lossless Q-factor consider (13) without the dissipation factor constraint. The problem is solved for each center position (x, y) of the embedded antenna (see Fig. 1). The optimization over arbitrary currents in (13) includes all possible antenna currents within the embedded antenna. It hence gives a lower bound on the Q-factor (see [15], [19]).

The choice of the embedded antenna position in (13) results in a partition of the impedance matrix into controllable and noncontrollable parts and appear here in the matrix $\mathbf{C}$ [see (11)]. Consequently, all the matrices appearing in (13) depend on the antenna position through (12). Given the impedance matrix and the stored energy matrices for the entire device, it is a small additional effort to determine the new position matrices through (12), which makes the computation of the position-dependent quantities comparatively fast. The domain is decomposed into a 10×10 equidistant grid for the center positions x, y of the embedded antenna within the upper left symmetry-corner of the terminal. Consequently, $x, y \in [10, 25]$ mm in ten equidistant steps, corresponding to the offset of the center from the nearest edge. The optimal FBW for each position at 850 and 900 MHz is shown in Fig. 2. It is calculated utilizing a reflection coefficient $|\Gamma_1| \leq 2^{-1/2}$ (-3 dB), resulting in FBW $\approx 2/Q$. If another maximal reflection coefficient $|\Gamma_2|$ is desired, it is easy to rescale the FBW

$$\mathrm{FBW}_2 \approx \mathrm{FBW}_1 \frac{|\Gamma_2|\sqrt{1-|\Gamma_1|^2}}{|\Gamma_1|\sqrt{1-|\Gamma_2|^2}} \tag{14}$$

which follows from (1).

From the optimization result at 850 and 900 MHz, it is clear that for this geometry and frequencies, the optimal bandwidth positions are at any of the four corner positions of the device and that the edges are the "second" best position. The Q-factor in the corner at 900 MHz is about 43, whereas a center position on the edge gives ∼61. In the center of the device, it is greater than 900. It is clear that the 900 MHz band due to its larger electrical size has a slightly improved FBW as compared with the 850 MHz case for the respective embedded antenna positions.

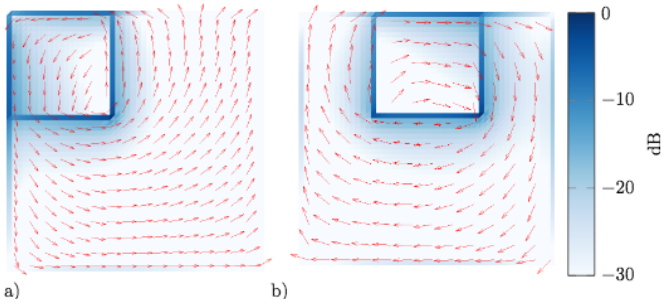

Fig. 3. Optimal current distribution for (a) corner and (b) center-edge embedded antennas, respectively, at 900 MHz. The figures have unit length current arrows, as a time-frozen sample of $\boldsymbol{J}(\boldsymbol{r}, t)$ to illustrate the current direction. The background color reflect $|\boldsymbol{J}(\boldsymbol{r}, \omega)|/|\boldsymbol{J}(\boldsymbol{r}, \omega)|_{\max}$ with a colorbar in dB to the right of the figure.

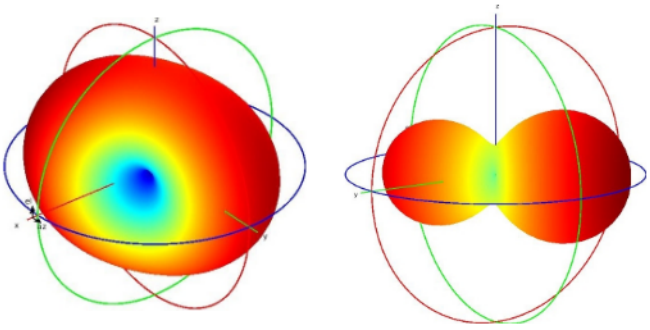

Fig. 4. Normalized radiation pattern for an optimal corner (left) and a center-edge (right) embedded current at 900 MHz, the color range is from -6 (blue) to 0 dB (red).

This example clearly shows that the corner position is the optimal position for an embedded antenna with this geometry and in the limit of electrically small devices. This observations certainly agrees with the design practice for small antennas and phones, where the embedded antenna often is placed at the outer edges of the terminal, with the additional information about the best avail bandwidth. The method here furthermore gives quantitative information about how much better a certain edge or corner position is, as compared to interior positions, information that usually is not available with other methods.

Fig. 3 depicts two optimized surface-currents distribution. Recall that the optimal current does not have to be unique, e.g., the minimum is unique, but there can be more than one minimizer. Since the structure has reflection symmetry planes for the illustrated currents, it is clear that the mirror-symmetric currents also give the same minimum Q factor. Fig. 4 shows the radiation pattern associated with the optimal currents in Fig. 3 for the corner and the edge position, respectively.

B. Bandwidth With Losses

Pure metal antennas tend to have rather small losses, and antennas on a very thin substrate can to leading order be approximated as pure metal antennas. The Ohmic losses are here modeled with a perturbation approach [24], resulting in the dissipation constraint in (13). From the lossless case considered above, note that the most interesting embedding region for the antenna is along the edge of the terminal. The investigations below thus focus on antennas positioned along the edge.

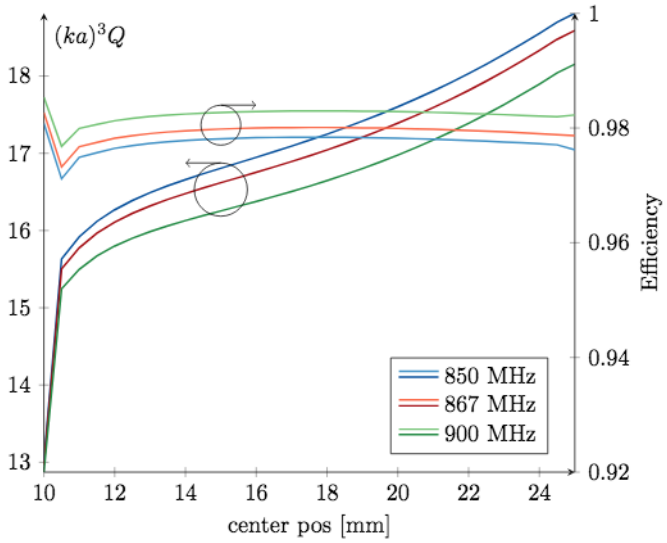

Fig. 5. Lower bound on the electrically normalized Q-factor (left) and the "default efficiency" (right) at [850, 867, and 900] MHz as a function of the embedded antennas center position along the edge.

In solving (13), it is clear that a sufficiently large δ_0 makes the constraint inactive. Such solutions have a dissipation δ and an efficiency $e = (1+\delta)^{-1}$ that is here called the "default efficiency" for a given embedded antenna configuration. This current solution(s) for the default efficiency is the same minimum solution and current distribution(s), as the solution determined in Section III-A, but now for Q_{rad}. The total Q-factor is, in this case, $Q = eQ_{\text{rad}}$. The efficiency depends on the materials and for a pure copper conductivity, $\sigma = 5.8 \cdot 10^7$ S/m, the calculations show that the efficiency e at all edge positions are $e = (1+\delta)^{-1} \geq 97\%$, where $\delta = R_{\text{s}}(\mathbf{I}_1^H \Psi \mathbf{I}_1)/(\mathbf{I}^H \mathbf{R} \mathbf{I})$ (see Fig. 5). This result was obtained by using a two-sided resistivity model based on the electrical skin-depth $R_{\text{s}} = (2\sigma\delta)^{-1}$, similar to EM-software conductivity models for an infinitesimally thin copper sheet. Fig. 5 depicts $(ka)^3 Q_{\text{rad}}$ for [850, 867, and 900] MHz together with the associated efficiency for an optimal solution. It is interesting to observe that the $(ka)^3$-scaling, with a being the radius of the terminal, still captures the main frequency variation. Note that this normalization is better for an embedded antenna at the corner position than at the other edge positions. This observation conforms with that the fact that the corner-position has a lower Q-factor associated with better utilization of the full terminal structure at these frequencies.

The best Q-factor currents (see Fig. 3) have their largest-amplitude currents at the edge of the embedded antenna region Ω_1. Thus, perturbations in this region could impact on the result. The here used RWG basis functions, representing the current density, has a small spatial extension corresponding to its support. The number of basis functions included in the "inside" the antenna domain, as well as their mesh-dependent shape and orientation, could thus modify the FBW result to a small extent.

To study this, consider a terminal with 101 equidistant points on the edge of the terminal, corresponding to 29 800 basis functions. A small position shift across a mesh boundary of the embedded is associated with an uncertainty, FBW $\sim (3.76 \pm 0.01)\%$ at 900 MHz for center-$x = 12$ mm and with a -3 dB reflection coefficient. This uncertainty is small, but to circumvent such a mesh-dependent influence, the simulations are done for a choice of embedded antenna positions such that the number of basis functions within the embedded antenna is constant.

In the optimization problem (13), it is possible to increase the antenna efficiency higher than the default efficiency. However, note that the default efficiency case is higher than the corresponding simulated and manufactured antenna (see Section IV). This is not surprising since the conductivity used here, is for the pure copper-case, whereas the manufactured antenna has a given surface-roughness and a thin dielectric layer in addition to the battery and electronic components. It is further known that it is challenging to reach up to an optimal antenna efficiency [29] since high-efficiency currents tend to be as homogeneous as possible (see [50]).

C. Optimal Bandwidth Position With Respect to Frequency

The result in Section III-A indicates that the bandwidth optimal corner position is stable under small perturbations in frequency. To further examine this design stability, consider the lossless optimal embedded position for frequencies between [850, 1900] MHz corresponding to the electrical sizes $ka = [0.62, 1.41]$. In the latter part of this range, the terminal is not electrically small. However, the antenna by itself is only $ka = 0.56$, and it is hence electrically small. The normalized FBWs are depicted in Fig. 1. The FBW is normalized with the maximal FBW for each frequency to emphasize the visibility of the optimal position. Thus, in Fig. 6, the optimal position has a color-code corresponding to 1 (dark red), and all other positions are a fraction of this maximum. To compare the results for 12 different frequencies in one figure, only one quadrant of the result for each frequency is shown. In Fig. 7, the FBW is depicted as a percentage.

It is clear from Figs. 6 and 7 that the corner position remains the optimal bandwidth position also for higher frequencies up to about 1.4 GHz. Here, note that the corner and an interior edge-point at $x \sim 20$ mm has a rather similar bandwidth FBW $\sim 20\%$. At higher frequencies, note that the optimal-bandwidth position moves toward the center of the edge. At 1.9 GHz, the center of the edge is the best bandwidth position (see Fig. 7). For all considered frequencies, the edge remains a much better bandwidth position to place the antenna than an interior point. Interior-points have roughly 50% or more in FBW reduction as compared to the optimal position.

IV. Antenna Design

A. Antenna Design and Simulation

The above theory thus predicts, in particular for sub-GHz frequencies, that it is substantially better to place the embedded antenna on the terminal edge rather than on an interior position, to obtain a larger bandwidth. The very best position

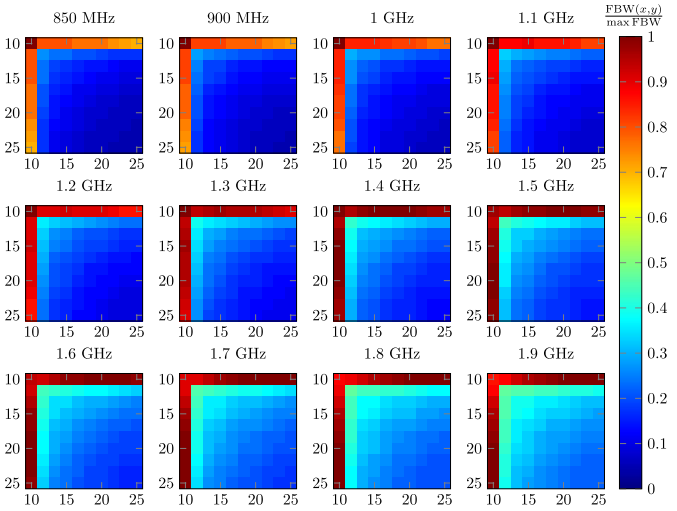

Fig. 6. Optimal FBW for antennas at different center-positions in the upper left corner as a function of frequency. The color-coding correspond to $\mathrm{FBW}(x, y)/\max \mathrm{FBW}$ at each frequency.

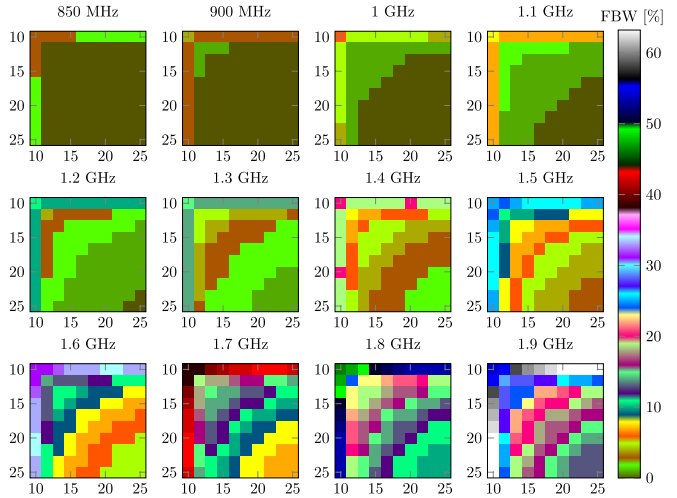

Fig. 7. Optimal FBW for antennas at different center-positions in the upper left as a function of frequency. The color-coding is the FBW in %.

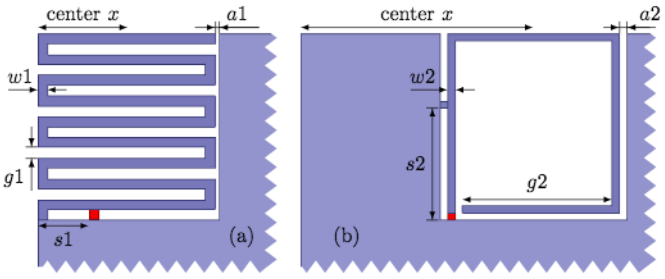

Fig. 8. Cutout drawings of the terminal for the embedded antenna models. (a) Meander antenna. (b) FIFA antenna.

TABLE I

OPTIMIZED ANTENNA PARAMETERS FOR THE EMBEDDED ANTENNAS IN FIG. 8

Meander Parameter	[mm]	FIFA Parameter	[mm]
a1	0.5	a2	0.78
g1	1.16	g2	16.1
s1	5.5	s2	11.8
w1	1.056	w2	0.85

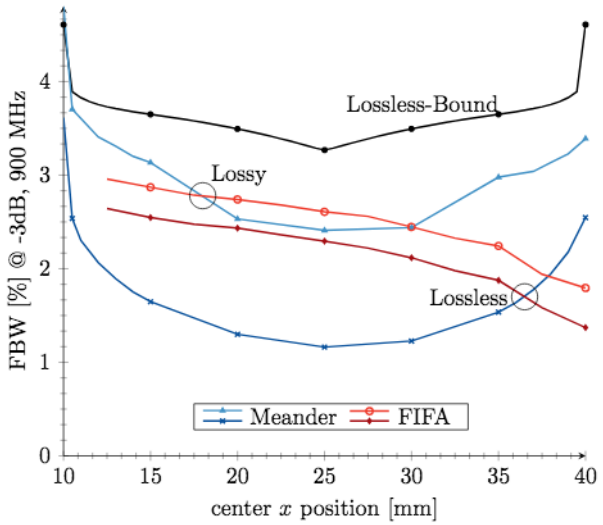

Fig. 9. FBW of the meander (blue) and the FIFA (red) in a planar terminal as a function of its center position along the edge at 900 MHz. The lossless (dark) and the lossy (light) cases are indicated. The feeding of the FIFA restricts the distance to the corner near the center $x = 10$ position.

is at the corner for this geometry and the sub-GHz frequencies, considered here. It is thus interesting to compare realized and measured embedded antennas with the physical bound. To do this, consider the bandwidth from a geometry optimized planar embedded meander antenna (see Fig. 8(a) and Table I). For each position on the upper terminal edge, an optimization-algorithm combined with a full-wave simulation in Ansys HFSS Release 2019 R3 is used to determine the best width and length of the meander, similar to [29], for each edge position to obtain the best possible bandwidth performance at 900 MHz.

Fig. 9 depicts both the simulated lossless meander and the bandwidth bound. Note that the corner position indeed is the best bandwidth position also for meander-antennas. However, there remains a gap for the meander antennas to reach the optimum bandwidth, as shown in Fig. 9.

Observe that a minimizing current, as shown in Fig. 3(b), shows that the currents rotate around the embedded antenna on the ground plane. This inspired us to consider the folded inverted F-antenna (FIFA) antenna, shown in Fig. 8(b), to excite the currents in a similar way. Its defining parameters are the linewidth, and the gap between the line and the ground-plane. Optimizing these parameters, with respect to maximum bandwidth at 900 MHz, results in the geometry shown in Fig. 8(b) and Table I. The matching stub shown on the left side of the FIFA adjusts the impedance to 50 Ω. The optimized geometry parameters for the meander at the corner and the FIFA antenna at the center of the edge are shown in Table I.

The simulated vector current is depicted in Fig. 10, it confirms that the proposed FIFA has a similar current distribution as the optimal solution Fig. 3(b). Its FBW is depicted as

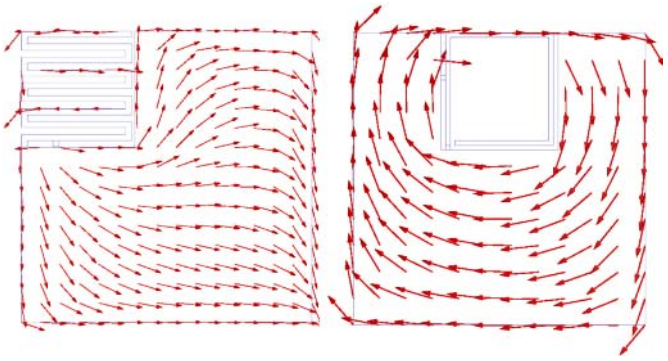

Fig. 10. Unit-length normalized current vector at the resonance frequency for the meander antenna (left) and the FIFA (right).

a function of the center position in Fig. 9 (red), and it is compared with the bound and the meander antenna (blue). We observe that for the FIFA has a better FBW for most of the considered position, apart from the meander in the corner. For an embedded antenna designed in this position of a device, the FIFA is a better choice than the meander, as it has twice as large −3 dB FBW (see Fig. 9). Although it is much better than the meander antenna at the center edge position, it still has some distance to the physical bound. The asymmetry with respect to $x = 25$ mm in the red and blue curves in Fig. 9 is due to the asymmetric feeding position and the matching stub (see Fig. 8).

B. Antenna Fabrication

To assess the predicted performance, prototypes for both the meander and the FIFA are manufactured. To minimize the dielectric effects, a 50 μm thick polyimide substrate is used as a supporting layer. A flexible printed circuit board is designed to connect the antenna to a UHF transceiver module (SX1276 from Semtech). To control the transceiver, a microcontroller that is mounted on a miniature PCB (ATMega 328p) is also integrated with the flexible terminal. The different electronic components are powered by a miniature Lithium battery with a $38 \times 19 \times 8$ mm^3 volume (see Fig. 11).

Considering that the electronic components and battery are positioned over the ground plane of the antenna, the influence on the antenna performance is limited. However, it can be seen in Fig. 12 that an average of a 6% downshift is observed due to the components and the dielectric.

The prototype is fabricated on a single-side PCB, the effect of a removed-copper trace inserted in the ground plane needs to be carefully considered: the signal line connecting the antenna input to the transceiver RF pin (top Fig. 11) is interrupting the conductivity continuity of the ground plane around the antenna feed and change the current distribution. In order to correct this effect, air-bridges (made with simple copper wires) are inserted to connect the two sides of the ground plane above the signal trace.

C. Antenna Measurement

Small antennas are difficult to measure because any cable connected to the device will strongly influence both the radiation pattern and its impedance. To address this issue, the transceiver is here placed on the terminal. It is used to generate a continuous wave (CW) with a 14 dBm output power. This methodology that was presented in [3] is here used to extract the realized gain and the total efficiency from a total radiated power (TRP) measurement. Radiation measurements are performed for different frequencies, and a −3 dB frequency bandwidth can be extracted from the total efficiency.

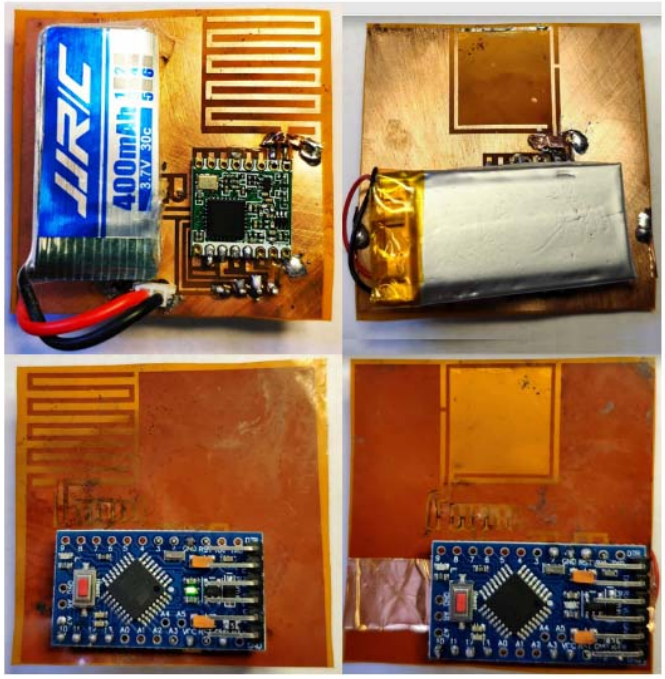

Fig. 11. Picture of terminal prototype for the meander antenna (left) and for the FIFA (right).

For the here manufactured prototypes, there is a resonance frequency downshift from 900 to 851 and 867 MHz for the meander and the FIFA, respectively. This frequency is downshifted due to the dielectrics, the presence of the electronic components, and the battery, together with the fabrication tolerance. To show this, the complete manufactured geometry is simulated and compared with the planar structure. The result is depicted in Fig. 12, where the downshift is clearly seen. The realized gain and total efficiency versus a frequency normalized by the resonance frequency, are presented in Fig. 13 for the meander and FIFA, respectively.

A −3 dB bandwidth of 43 (5.1% FBW) and 23 MHz (2.6% FBW) are extracted for the meandered and the FIFA, respectively. A good agreement with simulation is obtained. The measured 3-D-radiation pattern of the two prototypes are presented in Fig. 14. A good agreement is obtained with the predicted optimal radiation pattern in particular for the corner position, see Fig. 4. The optimal FIFA has a radiation pattern that is similarly oriented but with a less pronounced dumbbell-shape.

V. Discussion: Antenna Performance Comparison

Above, antenna designs have been developed from a planar lossless bound as compared with EM software-simulation

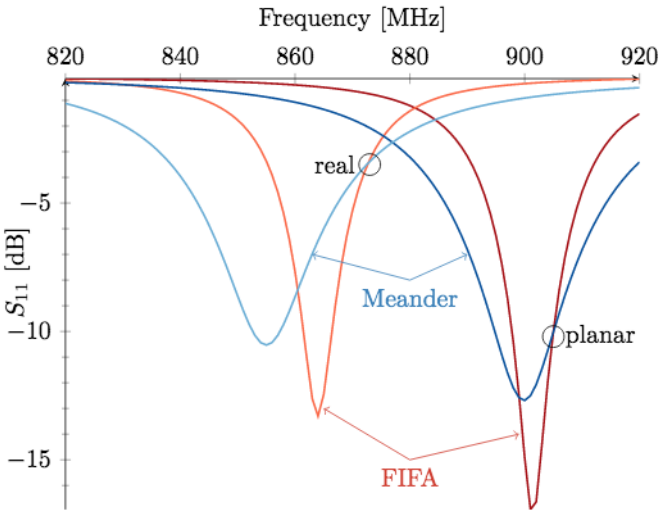

Fig. 12. Comparison between the planar structure (planar) and the structure with the electronic components (real) for both the meander (red) and FIFA (blue). The down-shift in frequency due to the dielectric and the components is clear.

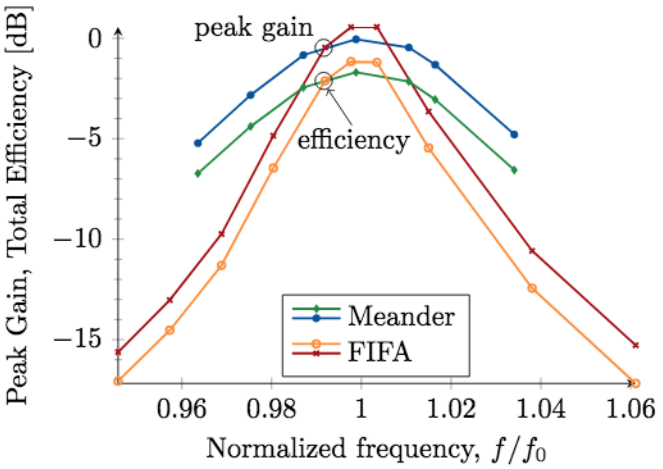

Fig. 13. Measured realized gain (blue) and total efficiency (green) for the meander with resonant frequency $f_0 = 851$ MHz. Measured realized gain (red) and total efficiency (orange) for the FIFA with $f_0 = 867$ MHz.

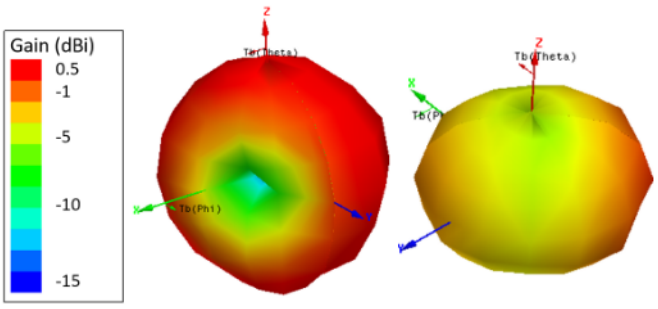

Fig. 14. Measured 3-D-radiation pattern at the resonance frequency for (left) the meander antenna and (right) the FIFA.

of planar lossless and lossy meander and FIFA embedded antennas Fig. 9. It is clear that the here simulated lossless antennas have FBW-bound−FBW-antenna $\geq$1% at 900 MHz

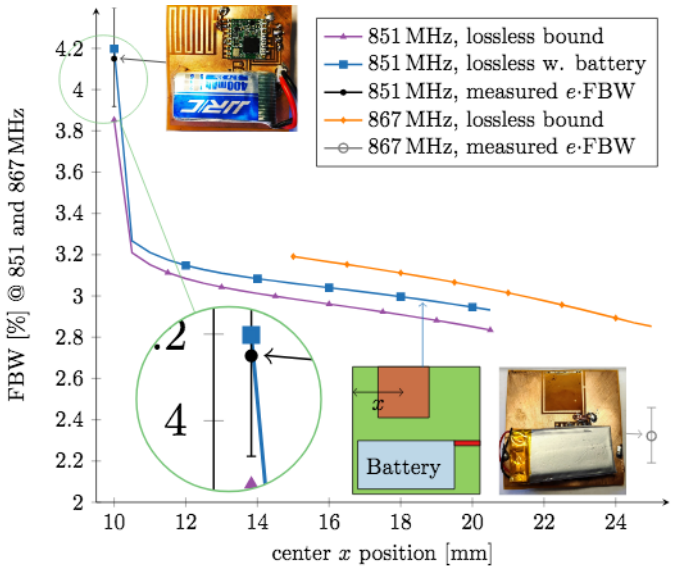

Fig. 15. 867 MHz lossless bound (orange) and the corresponding FIFA measurement FBW$*e$ (gray) with error bars corresponding to a 0.5 dB uncertainty of the efficiency. The 851 MHz lossless bound (purple) and the bound with an added battery (blue) are compared with the meander-antenna measurement, FBW$*e$ (black) with error bars corresponding to 0.5 dB in efficiency uncertainty.

for all positions, there is hence room for antenna design improvements. The realized antennas are matched to 50 Ω, at the respective center frequency, such an additional constraint can shift the bandwidth somewhat downward. However, the results in [29] indicate that such an impedance constraint only weakly impact upon the factor, and consequently on the FBW.

Even though the antennas initially were designed for 900 MHz, the downshift, as discussed above to 851 (meander) and 867 MHz (FIFA) are due to the dielectrics and electronic components required new calculations for the bounds. The bounds were thus simulated also at the frequencies 851 and 867 MHz. Their associated FBWs as a function of the position on the edge are shown in Fig. 15 in purple at 851 MHz for the near embedded antenna with center at $x = 10$ mm, $y = 10$ mm region and in orange near the center at $x = 25$ mm for $y = 10$ mm at 867 MHz.

The FBW measurements are utilizing the electronic components to measure the antenna properties without connected cables and to mimic a real application. This introduces a small uncertainty of 0.5 dB in the measured efficiency. The obtained FBWs are, respectively, 5.1% for the meander antenna at 851 MHz and 2.6% for the FIFA embedded antenna at 867 MHz. The corresponding total efficiency is −1.7 dB respective −1.16 dB with ±0.5 dB uncertainty.

Clearly, it is nontrivial to compare the physical bound for a planar lossless structure with the measured terminal containing batteries and electronic components. One way to account for losses is to recall that $Q = eQ_{\text{rad}}$, thus the relation between the radiation FBW and a lossy FBW can be approximated by an efficiency normalization. Assuming that the efficiency is not externally constrained we find that the radiation and lossless

FBW are approximately equal, that is,

$$\mathrm{FBW_{LL}} \approx e_{\mathrm{M}} * \mathrm{FBW_{M}} \tag{15}$$

where $\mathrm{FBW_M}$ is the measured FBW and $\mathrm{FBW_{LL}}$ is the estimated lossless bandwidth from the measurement and e_{M} is the measured efficiency. The lossless-normalized measured FBWs are inserted into Fig. 15 as a black dot at $x = 10$ mm (meander) and as a gray circle at $x = 25$ mm (FIFA), well below the planar lossless bound.

A second factor is the measurement/simulation comparison between a planar lossless structure with a nonflat measured antenna device containing a battery, electronics, and dielectrics. First, note that the planar structure physical bound is depicted with purple and orange in Fig. 15. It is interesting to see that the measured meander is above the planar structure bound. To take into account the battery in the physical bound we construct a 3-D model, see the inset in Fig. 15. The battery is modeled as a box on the ground plane of dimensions $38 \times 19 \times 8$ mm with a thin, 2 mm wide bridge (red). The bound with this updated model for 851 MHz (blue) is shown in Fig. 15 and limits the measured results.

The meander antenna is above the planar bound, but slightly below the model that is determined with the battery. Thus, compensating for the difference in measured and estimated efficiency give a close prediction of the expected measured bandwidth behavior, for close to optimal antennas. An estimate of the measurement uncertainty is included in the figure bracketing the measurement point. It is pleasing to see that the measured meander is very close to bandwidth optimal.

It is also interesting to note that the measured efficiency for the FIFA at the center position is higher than the efficiency of the meander at the corner position. This does not agree with the "default" efficiency of the optimal bound (see Fig. 5) since here the corner position has a slightly higher efficiency than the edge-center position. In the simulations observe that the "default" efficiency away from the corner increases as the embedded antenna moves away from the corner. After a local max at $x = 17.5$ mm there is a slight decrease in efficiency, still well above the $x = 10.5$ mm position. However, these default efficiency variations are rather small [0.977%, 0.985%] (~ -0.17 dB). What is clear from these considerations is that not only does the shape of the embedded antenna impact the efficiency, but also on the embedded position of the antenna. Clearly, there remain open questions in how to obtain predictive efficiency estimates combined with bandwidth bounds for small antennas.

VI. Conclusion

In this article, we show how the theory of Q-factor limitations can be used to determine the optimal bandwidth position for an embedded antenna. As part of the analysis, we also obtain the tradeoff relations for different positions in a planar terminal and note that there is a sharp increase in the available bandwidth for embedded antennas away from the edges. Thus, to obtain the largest possible bandwidth in the investigated device for sub-GHz frequencies, it is essential to embed the antenna as close as possible to an edge and preferably at a corner of the device at low frequencies. We conclude that there are optimal bandwidth positions for embedded antennas and that they are rather robust for sub-GHz frequencies.

We also investigate the optimal position with respect to different working frequencies. For lower frequencies, the corner is the best position. Once the terminal diameter is above $\lambda/3$ in size, the interior points of the edges are optimal in the here considered cases. For multiband antennas, the optimal bandwidth position is more challenging, and it will depend on e.g., the choice of the examined frequency bands. For this reason, optimal bandwidth positioning for multiband antennas remains an open question.

Two types of embedded antennas, a meander, and a FIFA are simulated and positioned along the edge. Their simulated bandwidth performances are compared with the here determined physical bounds. This shows that the designed antennas are close to the bound at the edge and at the corner, respectively. These antennas are also manufactured and measured. We note that the planar lossless FBW bound as well as the model with the simplified battery well predicts the measured results, in particular for the meander.

Acknowledgment

The CREMANT is acknowledged for measurement support.

References

[1] X. Lu, P. Wang, D. Niyato, D. I. Kim, and Z. Han, "Wireless networks with RF energy harvesting: A contemporary survey," *IEEE Commun. Surveys Tuts.*, vol. 17, no. 2, pp. 757–789, 2nd Quart., 2015, doi: 10.1109/COMST.2014.2368999.

[2] O. Björkqvist, O. Dahlberg, G. Silver, C. I. Kolitsidas, O. Quevedo-Teruel, and B. L. G. Jonsson, "Wireless sensor network utilizing RF energy harvesting for smart building applications," *IEEE Antennas Propag. Mag.*, vol. 60, no. 5, pp. 124–136, Oct. 2018, doi: 10.1109/MAP.2018.2859196.

[3] C. Pham, F. Ferrero, M. Diop, L. Lizzi, O. Dieng, and O. Thiare, "Low-cost antenna technology for LPWAN IoT in rural applications," in *Proc. 7th IEEE Int. Workshop Adv. Sensors Interfaces (IWASI)*, Vieste, Italy, Jun. 2017, pp. 121–126, doi: 10.1109/IWASI.2017.7974231.

[4] S. Guha *et al.*, "Autowitness: Locating and tracking stolen property while tolerating GPS and radio outages," *ACM Trans. Sensor Netw.*, vol. 8, no. 4, p. 31, 2012, doi: 10.1145/2240116.2240120.

[5] K. Diallo, A. NGom, A. Diallo, J. M. Ribero, I. Dioum, and S. Ouya, "Efficient dual-band PIFA antenna for the Internet of Things (IoT)," in *Proc. IEEE Conf. Antenna Meas. Appl. (CAMA)*, Västerås, Sweden, Sep. 2018, pp. 1–4, doi: 10.1109/CAMA.2018.8530584.

[6] H. Jaafar, D. Lemur, S. Collardey, and A. Sharaiha, "Parametric optimization of a non-foster circuit embedded in an electrically small antenna for wideband and efficient performance," *IEEE Trans. Antennas Propag.*, vol. 67, no. 6, pp. 3619–3628, Jun. 2019, doi: 10.1109/TAP.2019.2902614.

[7] J. Schlienz and D. Raddino. (2016). Narrowband Internet of Things whitepaper. Rode&Schwarz. [Online]. Available: https://cdn.rohde-schwarz.com/pws/dl_downloads/dl_application/application_notes/1ma266/1MA266_0e_NB_IoT.pdf

[8] T. Adiono *et al.*, "Development of long-range communication system for fishermen: An initial study," in *Proc. Int. Conf. ICT Rural Develop. (IC-ICTRuDev)*, Badung Regency, Indonesia, Oct. 2018, pp. 12–17, doi: 10.1109/ICICTR.2018.8706564.

[9] K. Schab *et al.*, "Energy stored by radiating systems," *IEEE Access*, vol. 6, pp. 10553–10568, 2018, doi: 10.1109/ACCESS.2018.2807922.

[10] A. D. Yaghjian and S. R. Best, "Impedance, bandwidth, and Q of antennas," *IEEE Trans. Antennas Propag.*, vol. 53, no. 4, pp. 1298–1324, Apr. 2005, doi: 10.1109/TAP.2005.844443.

[11] M. Gustafsson and B. L. G. Jonsson, "Antenna Q and stored energy expressed in the fields, currents, and input impedance," *IEEE Trans. Antennas Propag.*, vol. 63, no. 1, pp. 240–249, Jan. 2015. doi: 10.1109/TAP.2014.2368111.

[12] A. Ludvig-Osipov and B. L. G. Jonsson, "Stored energies and Q-factor of two-dimensionally periodic antenna arrays," *IEEE Trans. Antennas Propag.*, vol. 68, no. 8, pp. 5989–6002, Aug. 2020, doi: 10.1109/TAP.2020.2979482.
[13] A. Ludvig-Osipov and B. L. G. Jonsson, "Q-factor of periodic antenna arrays over ground plane," *IEEE Antennas Wireless Propag. Lett.*, vol. 19, no. 1, pp. 158–162, Jan. 2020, doi: 10.1109/LAWP.2019.2956420.
[14] A. Ludvig-Osipov, J.-M. Hannula, P. Naccachian, and B. L. G. Jonsson, "Physical limitations of phased array antennas," 2020, *arXiv:2006.02777*. [Online]. Available: http://arxiv.org/abs/2006.02777
[15] G. A. E. Vandenbosch, "Reactive energies, impedance, and Q factor of radiating structures," *IEEE Trans. Antennas Propag.*, vol. 58, no. 4, pp. 1112–1127, Apr. 2010, doi: 10.1109/TAP.2010.2041166.
[16] B. L. G. Jonsson and M. Gustafsson, "Stored energies in electric and magnetic current densities for small antennas," *Proc. Roy. Soc. A, Math., Phys. Eng. Sci.*, vol. 471, no. 2176, pp. 1–23, 2015, doi: 10.1098/rspa.2014.0897.
[17] M. Gustafsson and S. Nordebo, "Optimal antenna currents for Q, superdirectivity, and radiation patterns using convex optimization," *IEEE Trans. Antennas Propag.*, vol. 61, no. 3, pp. 1109–1118, Mar. 2013, doi: 10.1109/TAP.2012.2227656.
[18] B. L. G. Jonsson, S. Shi, L. Wang, F. Ferrero, and L. Lizzi, "On methods to determine bounds on the Q -Factor for a given directivity," *IEEE Trans. Antennas Propag.*, vol. 65, no. 11, pp. 5686–5696, Nov. 2017, doi: 10.1109/TAP.2017.2748383.
[19] M. Gustafsson, M. Cismasu, and B. L. G. Jonsson, "Physical bounds and optimal currents on antennas," *IEEE Trans. Antennas Propag.*, vol. 60, no. 6, pp. 2672–2681, Jun. 2012, doi: 10.1109/TAP.2012.2194658.
[20] M. Gustafsson and M. Capek, "Maximum gain, effective area, and directivity," *IEEE Trans. Antennas Propag.*, vol. 67, no. 8, pp. 5282–5293, Aug. 2019, doi: 10.1109/TAP.2019.2916760.
[21] S. Shi, L. Wang, and B. L. G. Jonsson, "Antenna current optimization and realizations for far-field pattern shaping," 2017, *arXiv:1711.09709*. [Online]. Available: http://arxiv.org/abs/1711.09709
[22] C. Ehrenborg and M. Gustafsson, "Fundamental bounds on MIMO antennas," *IEEE Antennas Wireless Propag. Lett.*, vol. 17, no. 1, pp. 21–24, Jan. 2018, doi: 10.1109/LAWP.2017.2772032.
[23] C. Ehrenborg and M. Gustafsson, "Physical bounds and radiation modes for MIMO antennas," *IEEE Trans. Antennas Propag.*, vol. 68, no. 6, pp. 4302–4311, Jun. 2020, doi: 10.1109/TAP.2020.2972398.
[24] L. Jelinek and M. Capek, "Optimal currents on arbitrarily shaped surfaces," *IEEE Trans. Antennas Propag.*, vol. 65, no. 1, pp. 329–341, Jan. 2017, doi: 10.1109/TAP.2016.2624735.
[25] M. Gustafsson, M. Capek, and K. Schab, "Tradeoff between antenna efficiency and Q-factor," *IEEE Trans. Antennas Propag.*, vol. 67, no. 4, pp. 2482–2493, Apr. 2019, doi: 10.1109/TAP.2019.2891448.
[26] M. Shahpari and D. V. Thiel, "Fundamental limitations for antenna radiation efficiency," *IEEE Trans. Antennas Propag.*, vol. 66, no. 8, pp. 3894–3901, Aug. 2018, doi: 10.1109/tap.2018.2836447.
[27] C. Pfeiffer, "Fundamental efficiency limits for small metallic antennas," *IEEE Trans. Antennas Propag.*, vol. 65, no. 4, pp. 1642–1650, Apr. 2017, doi: 10.1109/tap.2017.2670532.
[28] H. L. Thal, "Radiation efficiency limits for elementary antenna shapes," *IEEE Trans. Antennas Propag.*, vol. 66, no. 5, pp. 2179–2187, May 2018, doi: 10.1109/TAP.2018.2809507.
[29] M. Capek *et al.*, "Optimal planar electric dipole antennas: Searching for antennas reaching the fundamental bounds on selected metrics," *IEEE Antennas Propag. Mag.*, vol. 61, no. 4, pp. 19–29, Aug. 2019.
[30] D. Tayli, M. Capek, L. Akrou, V. Losenicky, L. Jelinek, and M. Gustafsson, "Accurate and efficient evaluation of characteristic modes," *IEEE Trans. Antennas Propag.*, vol. 66, no. 12, pp. 7066–7075, Dec. 2018, doi: 10.1109/TAP.2018.2869642.
[31] M. Cismasu and M. Gustafsson, "Antenna bandwidth optimization with single frequency simulation," *IEEE Trans. Antennas Propag.*, vol. 62, no. 3, pp. 1304–1311, Mar. 2014, doi: 10.1109/TAP.2013.2295426.
[32] S. R. Best, E. E. Altshuler, A. D. Yaghjian, J. M. McGinthy, and T. H. O'Donnell, "An impedance-matched 2-element superdirective array," *IEEE Antennas Wireless Propag. Lett.*, vol. 7, pp. 302–305, 2008, doi: 10.1109/lawp.2008.921372.
[33] C. Kolitsidas, "Next generation wideband antenna arrays for communications and radio astrophysics," Ph.D. dissertation, KTH Roy. Inst. Technol., Stockholm, Sweden, 2017.
[34] T. V. Hansen, O. S. Kim, and O. Breinbjerg, "Stored energy and quality factor of spherical wave functions–in relation to spherical antennas with material cores," *IEEE Trans. Antennas Propag.*, vol. 60, no. 3, pp. 1281–1290, Mar. 2012, doi: 10.1109/TAP.2011.2180330.
[35] S. R. Best, "Electrically small resonant planar antennas: Optimizing the quality factor and bandwidth," *IEEE Antennas Propag. Mag.*, vol. 57, no. 3, pp. 38–47, Jun. 2015, doi: 10.1109/MAP.2015.2437271.
[36] A. Clemente, M. Pigeon, L. Rudant, and C. Delaveaud, "Design of a super directive four-element compact antenna array using spherical wave expansion," *IEEE Trans. Antennas Propag.*, vol. 63, no. 11, pp. 4715–4722, Nov. 2015, doi: 10.1109/TAP.2015.2475617.
[37] Y. Huang and S. Zhang, "Complex matrix decomposition and quadratic programming," *Math. Oper. Res.*, vol. 32, no. 3, pp. 758–768, Aug. 2007, doi: 10.1287/moor.1070.0268.
[38] L. Lovasz, "On the Shannon capacity of a graph," *IEEE Trans. Inf. Theory*, vol. 25, no. 1, pp. 1–7, Jan. 1979, doi: 10.1109/TIT.1979.1055985.
[39] Z.-Q. Luo, W.-K. Ma, A. So, Y. Ye, and S. Zhang, "Semidefinite relaxation of quadratic optimization problems," *IEEE Signal Process. Mag.*, vol. 27, no. 3, pp. 20–34, May 2010, doi: 10.1109/MSP.2010.936019.
[40] M. Capek, M. Gustafsson, and K. Schab, "Minimization of antenna quality factor," *IEEE Trans. Antennas Propag.*, vol. 65, no. 8, pp. 4115–4123, Aug. 2017, doi: 10.1109/TAP.2017.2717478.
[41] F. Ferrero, L. Lizzi, B. L. G. Jonsson, and L. Wang, "A two-element parasitic antenna approaching the minimum Q-factor at a given directivity," 2017, *arXiv:1705.02281*. [Online]. Available: http://arxiv.org/abs/1705.02281
[42] J. Park and S. Boyd, "General heuristics for nonconvex quadratically constrained quadratic programming," 2017, *arXiv:1703.07870*. [Online]. Available: http://arxiv.org/abs/1703.07870
[43] B. L. G. Jonsson, "A comparison between QCQP-relaxation methods to determine a lower bound on a small antenna Q-factor," in *Proc. 13th Eur. Conf. Antennas Propag. (EuCAP)*, 2019, pp. 1–5.
[44] S. Rao, D. Wilton, and A. Glisson, "Electromagnetic scattering by surfaces of arbitrary shape," *IEEE Trans. Antennas Propag.*, vol. 30, no. 3, pp. 409–418, May 1982.
[45] M. Gustafsson, D. Tayli, C. Ehrenborg, M. Cismasu, and S. Nordebo, "Antenna current optimization using MATLAB and CVX," *FERMAT*, vol. 15, no. 5, pp. 1–29, 2016.
[46] J. D. Jackson, *Classical Electrodynamics*, 3rd ed. New York, NY, USA: Wiley, 1999.
[47] R. F. Harrington, "Effect of antenna size on gain, bandwidth, and efficiency," *J. Res. Nat. Bur. Standards D, Radio Propag.*, vol. 64D, pp. 1–12, Jan./Feb. 1960.
[48] B. L. G. Jonsson, "On directivity constraints and their influence on the lower Q-factor bound for embedded small antennas," in *Proc. Int. Conf. Electromagn. Adv. Appl. (ICEAA)*, Verona, Italy, Sep. 2017, pp. 1770–1773, doi: 10.1109/ICEAA.2017.8065639.
[49] G. J. Burke and A. J. Poggio, "Numerical electromagnetics code (NEC)-method of moments," Lawrence Livermore Nat. Lab., Livermore, CA, USA, Tech. Rep. ICID 18834, 1981. [Online]. Available: https://apps.dtic.mil/dtic/tr/fulltext/u2/a075289.pdf
[50] B. L. G. Jonsson and F. Ferrero, "On Q-factor bounds for lossy embedded antennas in electrically small devices," in *Proc. 13th Eur. Conf. Antennas Propag. (EUCAP)*, Krakow, Poland, 2019, pp. 1–4.

B. L. G. Jonsson received the Ph.D. degree in electromagnetic theory from the KTH Royal Institute of Technology, Stockholm, Sweden, in 2001.

He was a Post-Doctoral Fellow with the University of Toronto, Toronto, ON, Canada, and a Wissenschaftlicher Mitarbeiter (Postdoc) with ETH Zürich, Zürich, Switzerland. Since 2006, he has been with the Electromagnetic Engineering Laboratory, KTH Royal Institute of Technology. He has been a Professor in electromagnetic fields with the KTH Institute of Technology, since 2015. His research interest includes electromagnetic theory in a wide sense, including scattering, antenna theory, and nonlinear dynamics.

Fabien Ferrero (Senior Member, IEEE) received the Ph.D. degree in electrical engineering from the University of Nice Sophia Antipolis, Nice, France, in 2007.

From 2008 to 2009, he worked with the IMRA Europe (Aisin Seiki Research Center), Valbonne, France, as a Research Engineer, where he developed automotive antennas. In 2010, he was recruited as an Associate Professor with the Polytechnic School, University of Nice Sophia Antipolis. Since 2018, he has been a Full Professor with Université Côte d'Azur, Nice, where he is doing his research with the Laboratoire d'Electronique, Antennes et Télécommunications (LEAT). His studies concerns design and measurement of millimetric antennas, the Internet-of-Things (IoT) systems, and reconfigurable antennas.

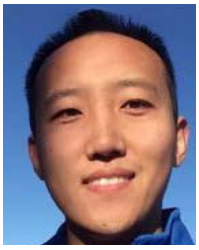

Shuai Shi was born in Shandong, China, in October 1989. He received the B.S. and M.S. degrees (as the Valedictorian) from Northwestern Polytechnical University, Xi'an, China, in 2011 and 2014, respectively, and the Ph.D. degree from the KTH Royal Institute of Technology, Stockholm, Sweden, in 2018.

Since 2018, he has been working at Ericsson AB, Stockholm, on radio system and antenna design. His research interests include antenna limitations, Q-factors, and optimal antenna design.

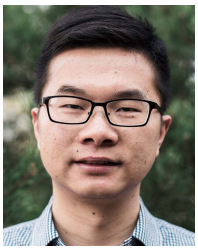

Lei Wang (Senior Member, IEEE) received the Ph.D. degree in electromagnetic field and microwave technology from Southeast University, Nanjing, China, in 2015.

From September 2014 to September 2016, he was a Research Fellow and a Post-Doctoral Researcher with the Laboratory of Electromagnetics and Antennas, Swiss Federal Institute of Technology (EPFL), Lausanne, Switzerland. From October 2016 to November 2017, he was a Post-Doctoral Research Fellow with the Electromagnetic Engineering Laboratory, KTH Royal Institute of Technology, Stockholm, Sweden. From November 2017 to February 2020, he was an Alexander von Humboldt Scholar with the Institute of Electromagnetic Theory, Hamburg University of Technology (TUHH), Hamburg, Germany. Since March 2020, he has been an Assistant Professor with the Institute of Sensors, Signals and Systems, Heriot-Watt University, Edinburgh, U.K. His research interests include the antenna theory and applications, active electronically scanning arrays, integrated antennas and arrays, substrate-integrated waveguide antennas, leaky-wave antennas, and wireless propagations.

Dr. Wang received the Chinese National Scholarship for his Ph.D. degree in 2014 and the Best Poster Award from the 2018 IEEE International Workshop on Antenna Technology (iWAT). He was granted the Swiss Government Excellence Scholarship to conduct research on SIW horn antennas and applications in 2014. He was also granted by the Alexander von Humboldt Research Foundation to take research on antenna modeling and optimization in 2016.